



**HAL**  
open science

## A Possible Dust Origin for an Unusual Feature in Io's Sodium Neutral Clouds

Cesare Grava, Timothy Cassidy, Nicholas M. Schneider, Hsiang-Wen Hsu, Jeffrey P. Morgenthaler, François Leblanc, Valeria Mangano, Kurt D. Retherford, Matthew H. Burger, Cesare Barbieri

► **To cite this version:**

Cesare Grava, Timothy Cassidy, Nicholas M. Schneider, Hsiang-Wen Hsu, Jeffrey P. Morgenthaler, et al.. A Possible Dust Origin for an Unusual Feature in Io's Sodium Neutral Clouds. *The Astronomical Journal*, 2021, 162 (5), pp.190. 10.3847/1538-3881/ac1ff8 . insu-03374890

**HAL Id: insu-03374890**

**<https://insu.hal.science/insu-03374890v1>**











Submitted on 1 Nov 2021

**HAL** is a multi-disciplinary open access archive for the deposit and dissemination of scientific research documents, whether they are published or not. The documents may come from teaching and research institutions in France or abroad, or from public or private research centers.

L'archive ouverte pluridisciplinaire **HAL**, est destinée au dépôt et à la diffusion de documents scientifiques de niveau recherche, publiés ou non, émanant des établissements d'enseignement et de recherche français ou étrangers, des laboratoires publics ou privés.

Copyright

## A possible dust origin for an unusual feature in Io's sodium neutral clouds

2 CESARE GRAVA <sup>1</sup>, TIMOTHY A. CASSIDY <sup>2</sup>, NICHOLAS M. SCHNEIDER <sup>2</sup>, HSIANG-WEN HSU <sup>2</sup>,  
3 JEFFREY P. MORGENTHALER <sup>3</sup>, FRANÇOIS LEBLANC <sup>4</sup>, VALERIA MANGANO <sup>5</sup>, KURT D. RETHERFORD <sup>1,6</sup>,  
4 MATTHEW H. BURGER <sup>7</sup> AND CESARE BARBIERI <sup>8</sup>

5 <sup>1</sup>*Southwest Research Institute, 6220 Culebra road, San Antonio, TX, 78238, USA*

6 <sup>2</sup>*Laboratory for Atmospheric and Space Physics, University of Colorado Boulder, Boulder, CO, USA*

7 <sup>3</sup>*Planetary Science Institute, Tucson, AZ, USA*

8 <sup>4</sup>*LATMOS/CNRS, Sorbonne Université, UVSQ, IPSL, Paris, France*

9 <sup>5</sup>*INAF/IAPS, Rome, Italy*

10 <sup>6</sup>*University of Texas at San Antonio, San Antonio, TX, USA*

11 <sup>7</sup>*Space Telescope Science Institute, Baltimore, MD, USA*

12 <sup>8</sup>*University of Padua, Department of Physics and Astronomy, Padua, Italy*

13 (Received June 1, 2019; Revised January 10, 2019; Accepted July 1, 2021)

14 Submitted to AJ

### 15 ABSTRACT

16 We report the results of model simulations performed to explain the nature of a sodium emission  
17 feature in Io Neutral Clouds. The feature was detected via high-resolution spectroscopic observations  
18 from the 3.6-meter Italian telescope TNG. The emission feature is blueshifted compared to the main  
19 emission (the banana-shaped Neutral Cloud of Io) by a few tens of km s<sup>-1</sup>, and it is most prominent  
20 when Io is a few tens of degrees before eclipse behind Jupiter's shadow. The feature's morphology  
21 changes with time, indicative of a geometrical effect. We constrained its direction, velocity, and column  
22 density with a model of sodium atom trajectories under the influence of Io's and Jupiter's gravity and  
23 solar radiation pressure. The model that best explains this emission feature has the atoms injected into  
24 the exosphere from the leading/sub-Jovian hemisphere of Io (45-68° West longitude), with velocities  
25 from 50 to 90 km s<sup>-1</sup> relative to Io. These trajectories are consistent with those of negatively charged  
26 dust grains (radius ~10 nm) accelerated by the co-rotational electric field of Jupiter's magnetosphere.  
27 We propose that sputtering of sodium atoms from Na-bearing molecules (NaCl and Na<sub>2</sub>SO<sub>4</sub>) in these  
28 nanodust grains is the process responsible for our emission feature. Both modeling and observational  
29 constraints provide an order-of-magnitude estimate of the sodium production rate of ~10<sup>26</sup> s<sup>-1</sup>. Our  
30 work provides another method to monitor the amount of material that Io is supplying to its Neutral  
31 Clouds and plasma torus.

32 *Keywords:* (not needed now)

### 33 1. INTRODUCTION

34 Io's Neutral Clouds are one of the brightest visible  
35 manifestations of the intense volcanic and magneto-  
36 spheric activity in the Jovian system. All the material  
37 that fills the Io Plasma Torus and Io's Neutral Clouds  
38 ultimately comes from the intense volcanic activity of

39 Io. Since the discovery of sodium at Io (Brown 1974),  
40 and its Neutral Cloud (Trafton et al. 1974), this mi-  
41 nor but bright species has been used to monitor the re-  
42 sponse of Io's Neutral Cloud to the changes of its drivers  
43 (Io volcanic activity and Jupiter magnetosphere). The  
44 resonant scattering efficiency (the so-called g-value) of  
45 sodium is orders of magnitude greater than the domi-  
46 nant species in Io's Neutral Clouds (S and O and their  
47 molecular compounds). Moreover, the wavelength of the  
48 sodium doublet (the D2 line at D1 line around 5900 Å)  
49 is such that it can be easily detected from the ground.

Over the past decades, observations and models have identified structures in the Neutral Clouds, each related to a particular source process and interaction with the Jovian magnetosphere. The most prominent of these structures, and the first to be discovered, is the corona, sometimes referred to as the “banana cloud” (the “Region B” in [Brown et al. 1975](#)), composed of slowly escaping sodium atoms (a few  $\text{km s}^{-1}$  relative to Io). Its peculiar morphology, with the leading part more extended (about  $60^\circ$  along the orbit) than the trailing part ( $30^\circ$  along the orbit), is controlled by celestial mechanics and by ionization from the plasma torus, which is warmer outwards from Io’s orbit compared to inwards ([Nash et al. 1986](#)). Another feature of the sodium Neutral Clouds is the “jet” (or directional feature; [Goldberg et al. 1984](#)), much more variable than the banana cloud, and composed of much more energetic atoms. The “jet” extends from Io in the anti-Jupiter direction, oriented approximately perpendicularly to the local Jovian magnetic field ([Wilson & Schneider 1994](#)). It is probably caused by prompt pickup ion neutralization very close to Io, its narrowness indicating an unperturbed Jovian magnetic field at Io ([Wilson & Schneider 1999](#)). The outer acceleration results from the corotational electric field applied to positively charged ions. Finally, a more diffuse feature is the “stream” ([Schneider et al. 1991](#)) of fast moving neutral sodium atoms resulting from dissociative recombination of fast molecular sodium-bearing ions (most likely  $\text{NaCl}^+$ ) corotating with Jupiter at  $\sim 70 \text{ km s}^{-1}$ . These atoms can be found all around Io’s orbit. Over many orbits around Jupiter, this stream creates the vast, faint neutral sodium cloud detected hundreds of Jupiter radii from Jupiter ([Mendillo et al. 1990](#)). All these features contribute to the roughly 1 ton of plasma that is injected in the Io Plasma Torus every second ([Schneider & Bagenal 2007](#)). Their morphology depends on several factors, including Io’s position (both orbital longitude and magnetic latitude) Jupiter’s magnetic field, and Io’s volcanic activity (see review by [Bagenal & Dols 2020](#)). For example, it has long been debated whether the sodium Neutral Clouds decrease in extent during eclipses behind Jupiter, due to condensation of Io’s atmosphere and/or to a suppression of solar photons available for photodissociation of sodium-bearing molecular compounds. It was to test these possibilities that we performed ground-based observations of Io before and after eclipses, in 2007. We discovered that solar flux is an important factor in supplying the sodium atoms to the Neutral Clouds, and that suppression of photo-dissociation of sodium-bearing molecules (most likely  $\text{NaCl}$ ) during eclipse drives a decrease in exospheric Na atoms soon after egress ([Grava et al. 2014](#)).

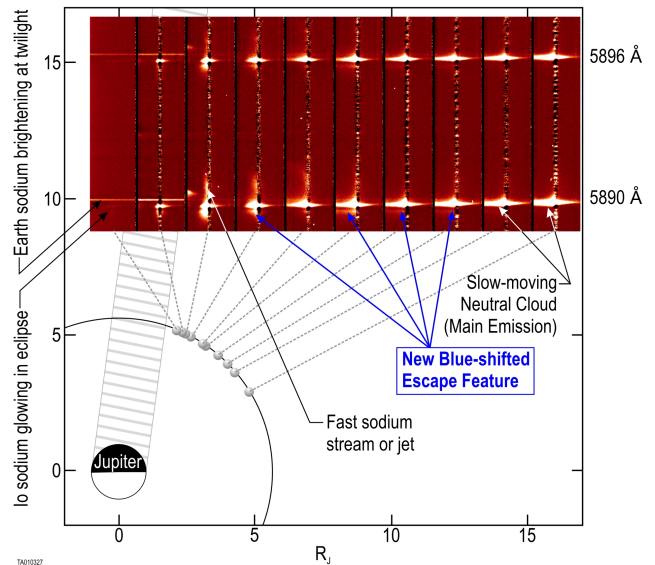


**Figure 1.** Two-dimensional spectra of Io with the continuum subtracted, stacked over a scheme of the observational geometry. The spectra progress in time from right to left, and wavelength run from bottom to top. The width of the spectra, corresponding to the length of the slit, is 27 arcsec.  $R_J$  = Jupiter radius  $\sim 70,000 \text{ km}$ . In the spectra, Jupiter direction is to the left of Io’s subtracted continuum.

During those observing runs, we also discovered an additional spectroscopic feature: an emission of sodium (visible at both D-lines) blueshifted (i.e., directed towards the observer and thus towards Jupiter) by tens of  $\text{km s}^{-1}$  relative to Io, hence moving much faster than the escape speed at Io (see Figure 1). We first reported this feature in [Schneider et al. \(2008\)](#) and performed additional observations at the same telescope in 2009. This paper describes the analysis of this feature using simulations of sodium atoms in Io’s Neutral Clouds and suggests possible explanations.

## 2. OBSERVATIONS AND DATA REDUCTION

Spectra were collected by the now-decommissioned high-resolution échelle spectrograph SARG mounted at the 3.6-meter Italian telescope TNG (Telescopio Nazionale Galileo) during several nights spanning 2 years, and different geometric configurations of Io. Spectra taken in 2007 were analyzed by [Grava et al. \(2014\)](#) and included in this work for completeness, while spectra taken in 2009 are analyzed here for the first time. The spectrograph’s slit was 26.7-arcsec long and 0.4-arcsec wide, had a spectral resolution of  $\lambda/\Delta\lambda \sim 115,000$ , and was placed almost always parallel to Jupiter’s rotational equator and centered on Io (or on other Galilean satellites, when used for calibration). The exposure time was almost always 600 s. The 2007 spectra were ob-

129 tained with an interference filter which blocked all pho-  
 130 tons but those with wavelengths close to the sodium  
 131 doublet. This procedure allowed to use the full extent  
 132 of the long slit without order overlapping. The 2009  
 133 spectra were obtained without such interference filter,  
 134 to collect light from the entire bandpass of SARG (3700-  
 135 10,000 Å) and to study therefore other species. As such,  
 136 only the central  $\sim 50$  pixels were used, and the remain-  
 137 ing  $\sim 30$  pixels at the edges were excluded due to order  
 138 contamination. The effective length of the slit in this  
 139 case was 17.7 arcsec.

140 Data reduction of the spectra was described in depth  
 141 in Grava et al. (2014) and is summarized here. Stan-  
 142 dard data reduction steps such as subtraction of bias,  
 143 flatfielding, and wavelength calibration (using a Th-Ar  
 144 lamp) were performed using IRAF routines. Specific  
 145 data reduction steps pertinent to our dataset were per-  
 146 formed later and included: 1) removal of an interference  
 147 pattern caused by the sodium filter (for 2007 observa-  
 148 tions only); 2) removal of a “pedestal” (residual back-  
 149 ground); 3) removal of a “ghost” of Jupiter’s spectrum  
 150 on top of Io spectra; 4) removal of telluric absorption,  
 151 performed using rapidly rotating O- and B-type stars  
 152 devoid of absorption lines observed at several airmasses  
 153 that bracketed ours; 5) subtraction of the “continuum”,  
 154 i.e. the solar light reflected off Io’s disk using spectra of  
 155 other Galilean satellites (Europa, Ganymede, and, more  
 156 rarely, Callisto) properly shifted to account for the dif-  
 157 ferent Doppler speeds; 6) conversion of sodium bright-  
 158 ness from counts  $\text{s}^{-1}$  to Rayleighs ( $1 \text{ R} = 10^6/4\pi$  photons  
 159  $\text{cm}^{-2} \text{ s}^{-1} \text{ sr}^{-1}$ ; Hunten et al. (1956)) using Jupiter spec-  
 160 tra and the well-measured intrinsic brightness of Jupiter  
 161 at the sodium wavelength ( $5.5 \text{ MR } \text{Å}^{-1}$ ; Brown & Schnei-  
 162 der 1981). During most of the nights the seeing was  
 163 good, never exceeding 1.6 arcsec as FWHM (calculated  
 164 as a deconvolution of a Gaussian fit to Io’s continuum  
 165 and the theoretical diameter of Io’s disk, 1.2 arcsec).  
 166 Details of observations are summarized in Table 1.

### 168 3. THE BLUESHIFTED EMISSION FEATURE

169 Figure 2 shows a typical spectrum of Io. On the left  
 171 is the average of Io’s brightness over detector columns  
 172 31-33, corresponding to a distance of 1.7-2.9  $R_{\text{Io}}$  east-  
 173 wards on the sky plane (towards Jupiter, in this case)  
 174 of Io’s center ( $1 R_{\text{Io}} \sim 1820 \text{ km}$ ) and, in dashed line,  
 175 the g-values. The g-value (or g-factor) is the number of  
 176 solar photons resonantly scattered each second by each  
 177 sodium atom. In optically thin exospheres, like Io’s neu-  
 178 tral clouds, the brightness  $I$  (in Rayleighs) is directly  
 179 related to the line-of-sight column density  $N$  (in atoms  
 180  $\text{cm}^{-2}$ ) by the g-value  $g$  (Brown & Yung 1976):

$$I = g \cdot N \quad (1)$$

181 The g-value (expressed in photons atoms $^{-1} \text{ s}^{-1}$ ) is related  
 182 to the solar spectrum, and depends, among other things,  
 183 on the heliocentric radial velocity  $\Delta v$  of sodium atoms,  
 184 owing to the deep Fraunhofer absorption in the solar  
 185 spectrum Hunten et al. (1988). We used g-values for  
 186 sodium from Killen et al. (2009).  $\Delta v$  is measured in  
 187 our spectra by the Doppler shift  $\Delta\lambda$  of Io relative to the  
 188 reference wavelengths  $\lambda$  of the sodium D-lines (5889.95  
 189 and 5895.92 Å for the D2 and D1 line, respectively):

$$\Delta v = c \cdot \frac{\Delta\lambda}{\lambda} \quad (2)$$

190 where  $c$  is the speed of light. The resulting  $\Delta v$  is referred  
 191 to Io’s reference frame, which is in itself moving relative  
 192 to the Sun. An atom at rest at Io moving away from the  
 193 Sun (like at Western elongations) will “see” a redshifted  
 194 solar spectrum. Therefore, to properly convert bright-  
 195 ness into column densities it is necessary to blueshift the  
 196 g-values, i.e. shifting them towards negative velocities.  
 197 This is shown in Figure 2, panel a, which shows that  
 198 the “dip” in the emission line (in Rayleighs) at  $-5 \text{ km}$   
 199  $\text{s}^{-1}$  is caused by the “dip” of the Fraunhofer line of the  
 200 g-value at  $-2.5 \text{ km s}^{-1}$ . The resulting division gives the  
 201 column density without such “dip” (panel b), but with  
 202 a “bump” on the blue side of the peak (negative veloci-  
 203 ties). This is the new emission feature. It is reminiscent  
 204 of the “skirt” detected first by Trafton (1975) and then  
 205 by Cremonese et al. (1992) and interpreted by Trafton &  
 206 Macy (1977, 1978) to be due to sodium atoms streaming  
 207 away from Io at moderate speeds ( $18 \text{ km s}^{-1}$  at most)  
 208 in the leading direction. However, it is different from  
 209 that because the “bump” lies on the opposite side. Our  
 210 “bump” is more prominent on the short wavelength side  
 211 when Io is west of Jupiter. Moreover, as we shall see  
 212 briefly, the feature changes Doppler shift through the  
 213 night. Note that in our observations the West direction  
 214 corresponds to the orbital trailing side of Io. In terms  
 215 of plasma flow, the trailing side corresponds to the is  
 216 upstream side, and East is the leading (or downstream)  
 217 side.

218 We performed the conversion from brightness to col-  
 219 umn density for all of our 2D spectra. An example of  
 220 the resulting 2D spectra, together with the geometry of  
 221 the observation, is shown in Figure 3 (the others can be  
 222 found in the supplemental material). In this figure, Io  
 223 is about to enter Jupiter’s shadow and the main emis-  
 224 sion feature (the “banana cloud”), being approximately  
 225 at rest relative to Io (white horizontal dashed lines),  
 226 dominates the spectra. The faint, straight emission line  
 227 traversing the whole slit length is Earth’s sodium layer  
 228 at 90 km altitude resonantly scattering solar photons  
 229 shortly before dawn. The streak of diffuse emission very  
 230 close to Io on the Eastern side (negative  $R_{\text{Io}}$ ) extending  
 231

**Table 1.** List of observations.  $t$  = exposure time.  $ssl$  = subsolar longitude, counted Westward (or counterclockwise) on Io. It is also equivalent to Io's orbital longitude, with  $0^\circ$  corresponding to superior conjunction (Io opposite to Earth behind Jupiter) and  $90^\circ$  corresponding to Eastern elongation.  $\lambda_{III}$  and  $Mlat$  are Io's system III longitude and magnetic latitude, respectively.  $p.a.$  = position angle, or the slit's angle relative to Jupiter's rotation axis, counted counterclockwise starting from Jupiter's north pole.

filename	obs. mid-time (UT)	t (s)	ssl ( $^\circ$ )	$\lambda_{III}$ ( $^\circ$ )	$Mlat$ ( $^\circ$ )	p.a. ( $^\circ$ )
JDEI0102	2007-04-25T02:01:33	600	316	29	-10	66
JDEI0106	2007-04-25T03:07:52	600	326	59	-8	66
JDEI0109	2007-04-25T03:39:07	600	330	74	-6	66
JDEI0112	2007-04-25T04:14:26	600	335	90	-4	66
JDEI0114	2007-04-25T04:50:26	600	340	107	-1	66
JDEI0115	2007-04-25T05:02:42	600	342	112	0	66
JDEI0119	2007-04-25T05:41:37	600	347	130	3	90
JDEI0120	2007-04-25T05:53:17	600	349	136	4	90
JDEI0121	2007-04-25T06:04:55	600	351	141	5	90
JDEI0122	2007-04-25T06:12:44	120	352	146	5	90
JDWF0002	2007-05-11T00:16:32	600	316	213	9	85
JDWF0004	2007-05-11T00:39:57	600	319	223	9	90
JDWF0008	2007-05-11T01:22:55	600	326	243	7	90
JDWF0010	2007-05-11T01:37:36	600	328	250	6	90
JDWF0015	2007-05-11T02:30:28	600	335	274	3	90
JDWF0017	2007-05-11T02:46:03	600	337	282	2	90
JDWF0022	2007-05-11T03:37:23	600	345	305	-2	90
JDWF0024	2007-05-11T03:52:34	600	347	312	-3	90
JDWF0025	2007-05-11T04:04:15	600	348	318	-4	90
JDWF0026	2007-05-11T04:18:16	600	350	324	-5	90
JFQI0034	2007-06-20T23:37:43	600	11	183	9	90
JFQI0035	2007-06-20T23:49:40	600	12	188	9	90
JFQI0037	2007-06-21T00:05:42	600	14	196	10	90
JFQI0043	2007-06-21T01:05:08	600	23	224	9	90
JFQI0045	2007-06-21T01:19:53	600	25	230	8	90
JFQI0049	2007-06-21T01:59:44	600	31	249	7	90
JFQI0051	2007-06-21T02:14:04	600	33	256	6	90
JFQI0056	2007-06-21T03:12:27	600	41	282	2	90
JFQI0058	2007-06-21T03:28:22	600	43	290	0	90
JGGV0044	2007-07-06T21:53:49	600	10	7	-9	90
JGGV0045	2007-07-06T22:05:48	600	12	13	-9	90
JGGV0049	2007-07-06T22:36:19	600	16	27	-10	90
JGGV0052	2007-07-06T23:06:43	600	21	41	-9	90
JGGV0058	2007-07-07T00:02:07	600	29	67	-7	90
JGGV0062	2007-07-07T00:36:20	600	33	83	-5	90
JGGV0067	2007-07-07T01:20:25	600	40	103	-1	90
KPBB0028	2009-09-07T21:55:26	180	234	86	-4	-270
KPBB0034	2009-09-07T23:38:40	600	249	132	3	-270
KPCB0056	2009-09-08T23:43:16	600	93	81	-5	-270
KPCB0059	2009-09-09T00:24:09	600	99	100	-2	-180
KPFB0035	2009-09-09T20:22:05	600	268	296	-1	-270
KPFB0038	2009-09-09T20:59:06	600	273	313	-3	-180
KPFB0041	2009-09-09T21:33:50	600	278	329	-6	-270
KPFB0047	2009-09-09T22:27:46	600	286	353	-8	-270
KPIB0078	2009-09-12T23:43:39	600	187	230	9	-180
KPIB0081	2009-09-13T00:25:12	600	193	249	7	-270
KPJB0031	2009-09-13T21:33:57	600	12	116	1	-270
KPJB0033	2009-09-13T21:51:41	600	14	124	2	-270
KPJB0050	2009-09-14T01:30:31	600	45	226	9	-270

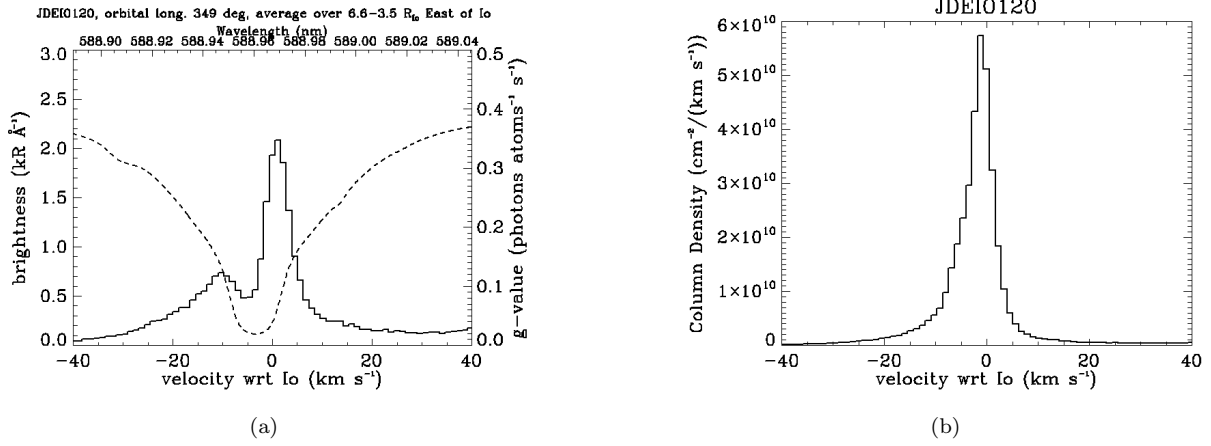


**Figure 2.** Left: spectrum of one Io observation (solid line) and the g-value used (dashed line) around the D2 emission line. Right: their ratio, which is the column density.

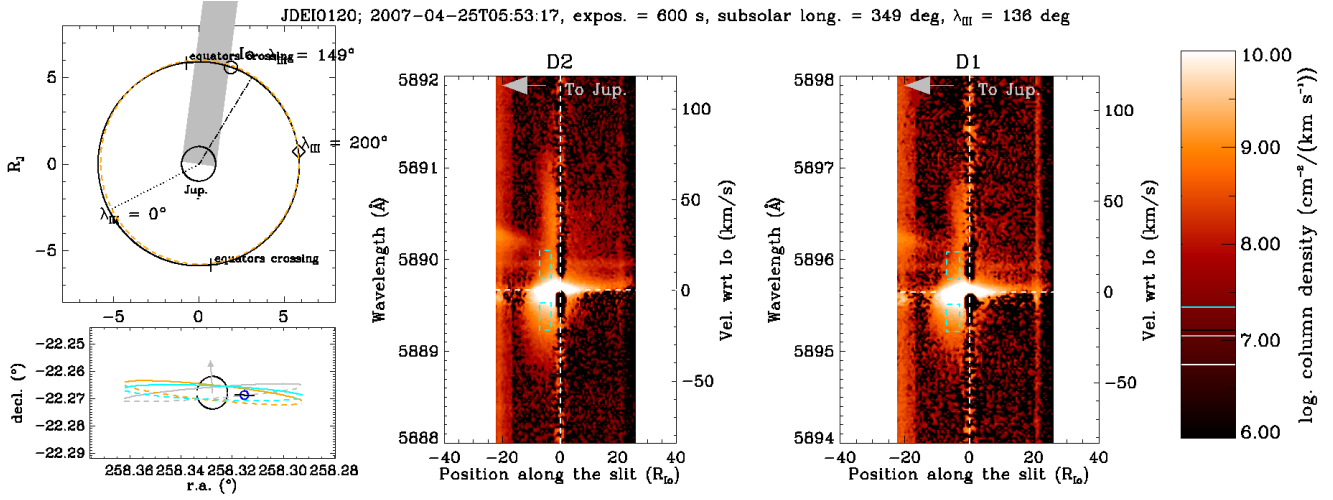


**Figure 3.** Composite image to put our 2D spectra in the observational perspective. The two right panels show our 2D Io spectra converted into column densities, in logarithmic color scale (D2 and D1, respectively). The region enclosed within the cyan dashed rectangles (7-22 km s<sup>-1</sup> and 3-7 Io radii) is used to compute the average source rate discussed in Section 5 and listed in Table 2. The gray arrows indicate the direction to Jupiter (towards right, in this case). The left panels show a simplified view of the geometry of the observations, from the celestial north pole (top) and from Earth (bottom), similar to Cremonese et al. (1992). Black solid circle on top (and gray on bottom) represents Io's orbit, in Jupiter's equatorial plane. Orange dashed circles on both top and bottom left panels represent Jupiter's magnetic equator at Io's distance, and include the tilt of 9.8° towards System III magnetic longitude  $\lambda_{III} = 200^\circ$  and the offset of 0.12  $R_J$  towards  $\lambda_{III} = 149^\circ$ . Cyan circle in bottom left panel represents the centrifugal equator, where the cold plasma ions reside. The arrow in the lower left panel indicates the rotation axis of Jupiter, and is black or gray if it points towards or away from the observer, respectively. Dashed lines in lower left panel indicate portions of the circles away from the observer. The blue circle and the small black line crossing it represent Io's disk and the spectrograph's slit, respectively. All objects in the two left panels are drawn to scale, except Io, for which the size has been magnified by 10. Corresponding images for the other observations can be found in the supplemental material.

to  $\sim 75 \text{ km s}^{-1}$  is the stream of fast sodium atoms that feed the giant sodium nebula (e.g. Flynn et al. 1992). The feature modeled in this paper is the extended emission blueshifted by few of tens of  $\text{km s}^{-1}$  with respect to Io, meaning these sodium atoms are moving towards the observer. The feature is seen here in the eastern half of the slit (left, in the figure), i.e. towards Jupiter.

#### 4. MODELING THE EMISSION FEATURE

We applied our Monte Carlo model of sodium atom trajectories (Burger et al. 2014) to reproduce our observations as closely as possible, by including the location and direction of ejection and the velocity distribution of ejected atoms. These parameters are constrained by our observations. The goal is to reproduce the emission feature and its temporal variability.

Figure 4 illustrates the change in time of the new feature’s morphology at different orbital (or subsolar) longitudes. This sequence shows that the blue-shifted feature, more prominent towards the end of the observing run, early in the night is red-shifted by a similarly high speed ( $> 10 \text{ km s}^{-1}$ ). The transition from red to blue shifts suggests that Na is ejected in a direction that is roughly perpendicular to the Io-observer line when the subsolar longitude is  $\sim 330^\circ$  (between the 4<sup>th</sup> and the 5<sup>th</sup> spectrum in Figure 4). This red-to-blue shift can then be explained by the changing observing geometry as Io orbits Jupiter. This peculiar behavior inspired our modeling approach. We first modeled the trajectories of the neutral sodium atoms (Section 4.1) and then found a plausible physical mechanism that can bring these sodium atoms at the location and with the speed we observe them (Section 4.1).

##### 4.1. Neutral sodium atoms trajectories

To simulate the observations we used the Monte Carlo model that is described in Burger et al. (2014). In this model, atoms are tracked under the forces of gravity and solar radiation pressure. The equations of motion are solved with a 5<sup>th</sup> order, adaptive step-size Runge-Kutta algorithm. Atoms are ejected at randomly selected times between the start and end of the model run so that the simulation contains a mixture of freshly released and older atoms. Loss processes include photoionization, electron-impact ionization, and charge exchange, though the atoms in the simulations shown below are mostly lost by leaving the small field of view. The observation geometry was recreated using the SPICE toolkit (Acton 1996).

We ran the model many times with different initial conditions in order to determine the direction and speed of Na that would reproduce the red-to-blue shift in Figure 4. Sodium atoms are ejected radially in intervals

11.25° wide. The origin of the ejected atoms is labeled in Io’s West longitude, where  $0^\circ$  corresponds to the sub-Jupiter meridian and  $90^\circ$  points along Io’s orbital motion (the “leading” direction). Speeds values from 4 to  $130 \text{ km s}^{-1}$  were used, each with a narrow distribution (each bin being  $10 \text{ m s}^{-1}$  wide).

Each of the two free parameters we used to reproduce our observations affects only one aspect of the emission feature. The ejection speed distribution affects the Doppler shift (wavelength dimension), while the ejection location affects the morphology of the emission feature (spatial direction). This is illustrated in Figure 5, where we show the effects of changing these parameters, compared to the nominal, best model.

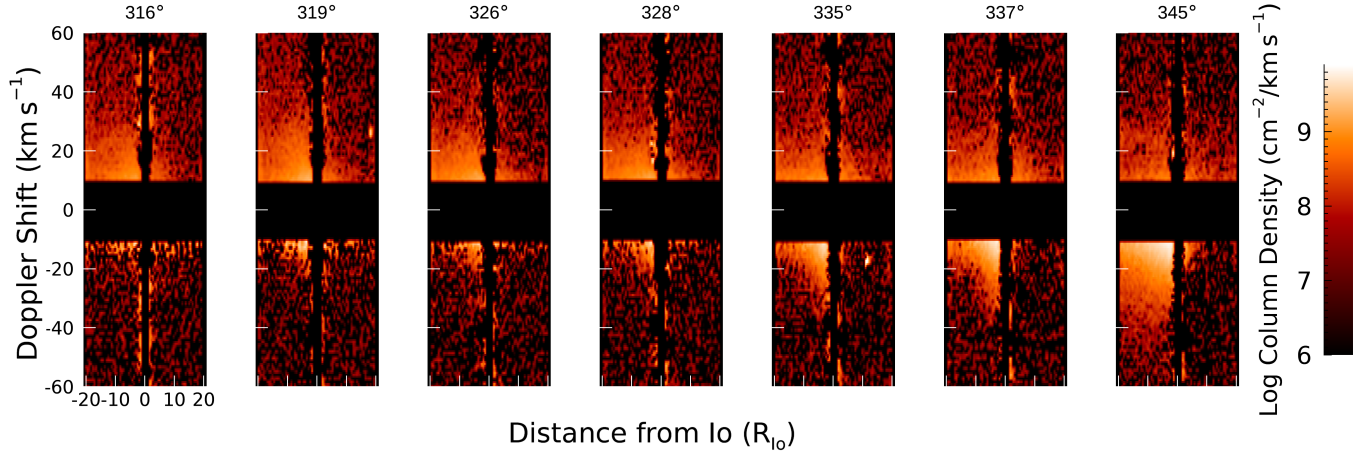
We find that the best combination of parameters to reproduce our observations is a broad speed distribution, with ejection velocities relative to Io of  $50\text{-}90 \text{ km s}^{-1}$ , and a relatively narrow range of ejection location:  $45\text{-}68^\circ$  of Io West longitude, meaning an ejection from the subjovian/leading hemisphere. Models with the nominal direction but lower speed ( $40 \text{ km s}^{-1}$ ) or higher speed ( $130 \text{ km s}^{-1}$ ) fail to match the magnitude of the Doppler shift, though they maintain the red-to-blue transition at a subsolar point of  $\sim 330^\circ$  (left-right panels in Figure 5). The mismatches in direction include one angular bin toward the leading direction and one bin toward the subjovian direction, and these both fail to reproduce the red-to-blue transition and the magnitude of the Doppler shift (top-down panels in Figure 5).

Figure 6 shows the best simulations compared to some of the observations. The rest of the data-model comparison can be found in the movie in the Supplemental Material. The nominal model shown here (in both Figure 5 and 6) includes speeds of  $57 \text{ km s}^{-1}$  and  $90 \text{ km s}^{-1}$ , though lower speeds could be included without significantly changing the result. Figure 6 illustrates how our model can reproduce the shift in velocity relative to Io (from red, or positive, to blue, or negative) within the same amount of time (about 4 hours).

Figure 7 shows a top-down view of the nominal model of sodium trajectories near the beginning and end of the observing sequence. In this image, directions toward the observer (Earth,  $\oplus$ ) and Jupiter ( $\text{♃}$ ) are indicated. The red-to-blue shift is seen here as a change in ejection direction as seen from Earth. Also, it can be noted that the ejection direction is roughly halfway, in terms of degrees, between the leading direction and Jupiter direction.

##### 4.2. Dust grains trajectories

Having found the characteristics of the sodium feature (speed distribution and direction), we need to identify



**Figure 4.** Observations taken in May 2007, calibrated in column density per unit velocity at different orbital (or subsolar) longitudes. Doppler velocities less than  $10 \text{ km s}^{-1}$ , which include the “banana cloud”, have been blacked out to highlight the feature, which transitions from red-shifted to blue-shifted in this 4-hour time span. Io’s orbital position is given as subsolar longitude and is indicated at the top of each plot. Io’s continuum has been carefully removed with the procedure discussed in the text.

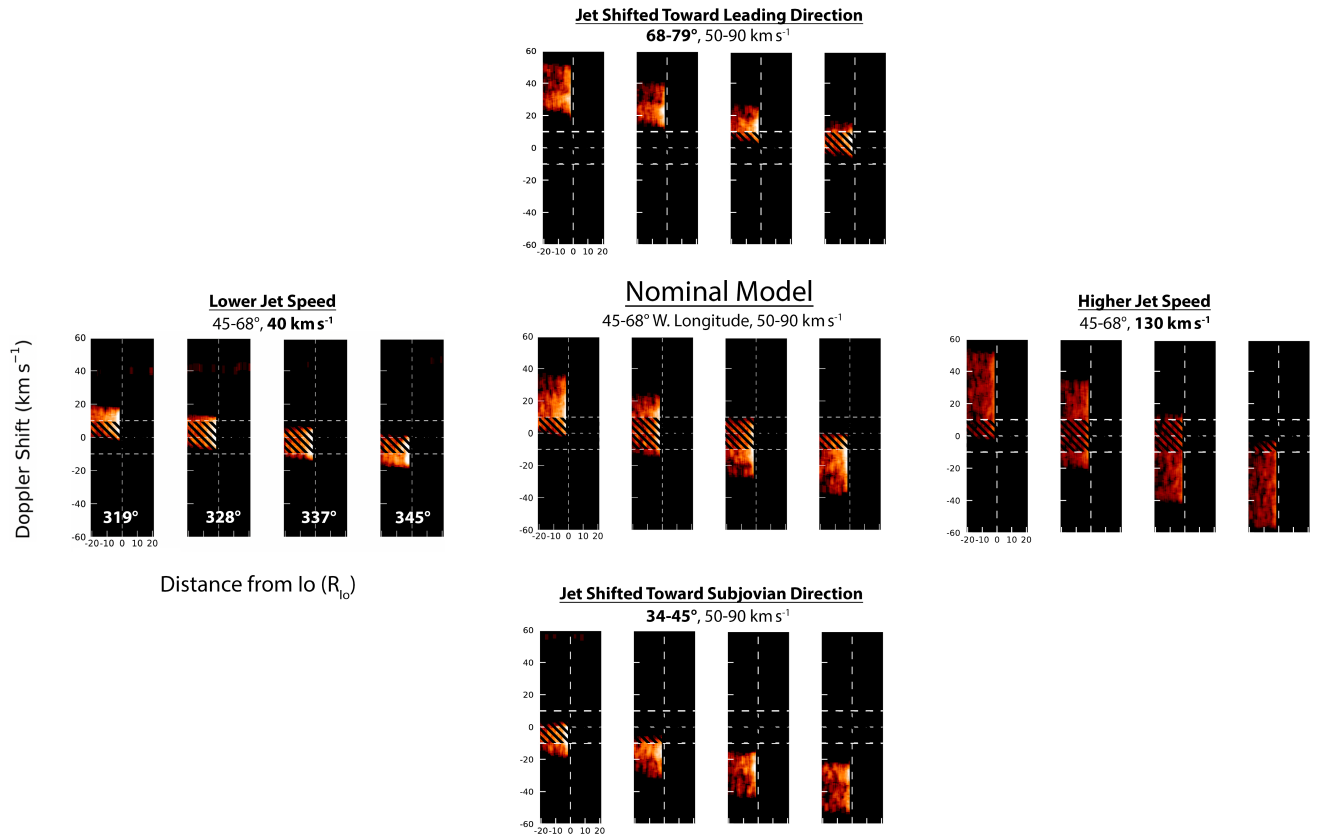


**Figure 5.** The simulation from the best model is shown at the center. The other four sub-panels show models with the right ejection direction but too low (left panel) or too fast (right panel) ejection speed, or models with the right ejection speed but wrong directions (top and bottom panels). Velocities within  $10 \text{ km s}^{-1}$ , marked by horizontal dashed lines, have been masked to leave out the main emission feature. The vertical dashed line represents the region of Io’s continuum.



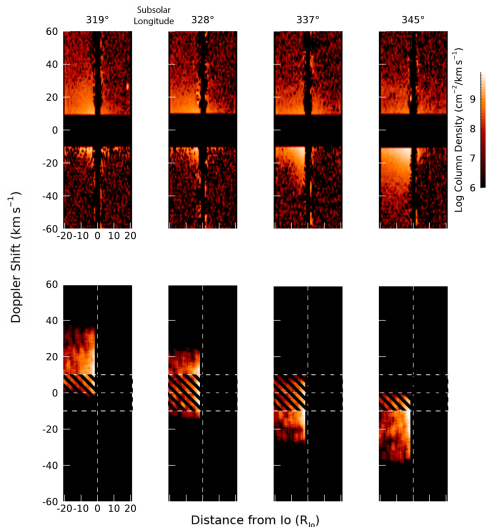


**Figure 6.** Comparison between four spectra in May 2007 (top panel) and their best fit model simulations (bottom panel). Note how the simulations are able to reproduce the shift in Doppler velocity, from positive relative velocities (moving away from the observer) to negative ones (moving towards the observer).

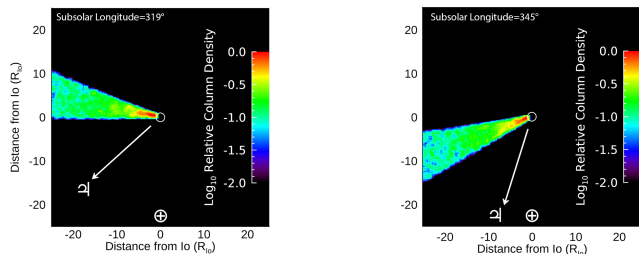


**Figure 7.** Top-down view of the model shown in Figure 6. The left panel shows the beginning of the observation sequence, when the Na is directed away from the observer to produce a red Doppler shift. The right panel shows the end of the sequence, when the Na is blue shifted. The white arrow points toward Jupiter, Earth is straight down.

a process that may bring sodium atoms at the location and speed observed. The direction of the blueshifted sodium feature (towards Jupiter) is consistent with negatively charged particles that move following Jupiter magnetosphere’s co-rotational electric field (e.g. Horányi et al. 1997). There are two possible candidates: sodium-bearing negative ions that are promptly neutralized and negatively charged Na-rich dust grains from which sodium atoms are liberated. In this section we discuss the latter, as many of the grains’ properties agree with our directional feature; at the end of Section 5.1 we briefly discuss the negative ions hypothesis.

Dust in the Jovian environment has been detected by multiple spacecraft: Ulysses (Grün et al. 1993), Galileo

(Grün et al. 1996), and Cassini (Postberg et al. 2006). All these observations are consistent with electrically charged dust grain of radius  $\sim 10$  nm (Zook et al. 1996). The periodicity of the dust impact signal in Galileo data was one of the early indicators that Io, and not the gossamer rings, was the source of such dust grains (Graps et al. 2000). Subsequently, the Cosmic Dust Analyser (CDA) onboard Cassini was able to distinguish the composition of these grains. NaCl was the dominant species identified by CDA, followed by other components like  $\text{Na}_2\text{SO}_4$  and  $\text{K}_2\text{SO}_4$  (Postberg et al. 2006). This is in contrast with the main composition of Io’s atmosphere and neutral clouds, where NaCl,  $\text{Na}^+$ , and  $\text{Cl}^+$  are just trace species (NaCl fraction in composition is less than 1%, while the  $\text{Na}^+$  and  $\text{Cl}^+$  concentration in the torus is between 2 and 6%; Lellouch et al. 2003; Küppers & Schneider 2000). The inverse trend in composition for dust may be related to the process that ultimately ejects these particles in the first place, i.e. volcanic eruptions. Because of their high condensation temperature, NaCl and KCl are abundant condensates 20 min after outgassing from the vent, while sulphuric components, due to their lower condensation temperature, are still far from condensation (Zhang et al. 2004).

We performed simulations of the trajectory of negatively charged nanodust grains of various sizes. We assume that the dust particles 10nm in radii start with a circular Keplerian motion at Io’s orbit and an initial charge of 20 electric charge, corresponding to a surface potential of -3 V. The charging and dynamical evolution of nanometer-sized grains is modeled as described in Horányi et al. (1997). For individual dust grains, two equations are integrated simultaneously: the equation of motion and the grain charging equation. The equation of motion considers the gravity of Jupiter and the Lorentz forces acting on the grain from the co-rotating magnetosphere. The grain charging equation depends on plasma properties at the grain’s location and determines the grain charge-to-mass ratio, essential to calculate the Lorentz forces. Grains can be charged negatively or positively, depending on the plasma environment, and the charging begins almost instantaneously.

A top-down view of the trajectory of a negatively charged dust grain of radius 10 nm, as well as a positively charged one (same size), is shown in Figure 8. Figure 9 shows the direction, the relative speed and distance with respect to Io of a negatively charged dust grain of radius 10 nm. The gray circle in that figure represents the parameter space (both velocity and distance to Io) consistent with our observations. The dynamical evolution of charged nanoparticles largely depends on the grain charge polarity: the positively charged parti-

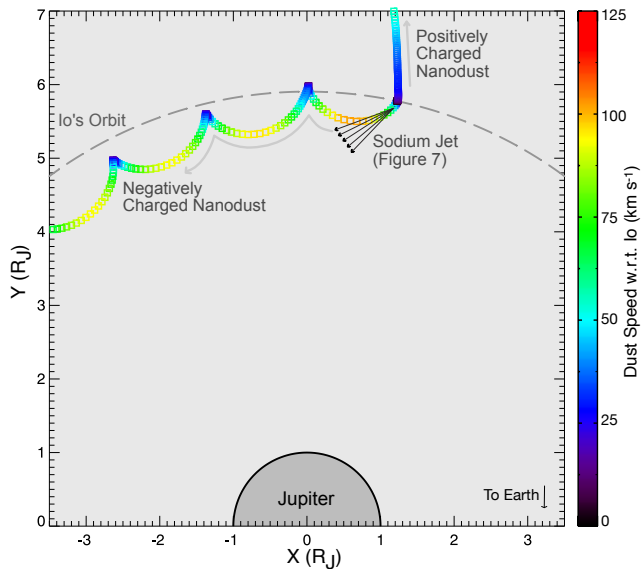


**Figure 8.** Top-down view of the trajectories of a negatively charged and a positively charged 10-nm-radius dust grain.  $R_J = \text{Jupiter radius} \sim 70,000 \text{ km}$ .

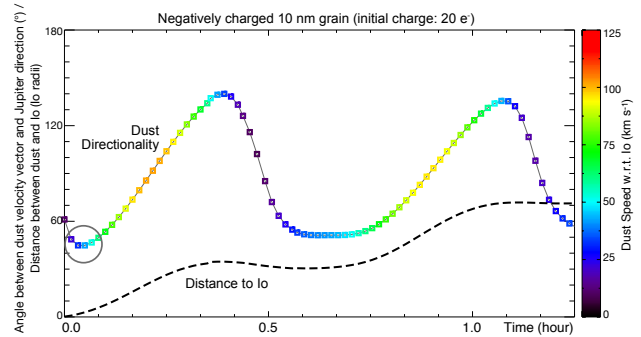


**Figure 9.** Simulation of trajectory of a negatively charged 10-nm-radius dust grain (of  $20 e^-$  initial charge) moving under the influence the co-rotational electric field of Jupiter's magnetosphere. The line threading through the colored squares is the direction (angle), while the colored squares represent the velocity. The gray circle indicates the parameter space of the modeled neutral sodium atoms: speed range of  $50\text{-}90 \text{ km s}^{-1}$  (cyan to yellow colors) and direction of  $\sim 45^\circ$ . The negatively charged particles have the right velocity at the right time to match our observations. The dashed line is the distance from Io and is also referred to the y axis (in Io radii) and that is also consistent with our data (Figure 4). Tick marks on the x axis are 5 minutes.

cle is accelerated away from Jupiter in almost a straight trajectory, while the negatively charged one exhibits a cycloidal motion along Io's orbit similar to pick-up ions. In general, negatively (positively) charged grains are accelerated towards (away from) Jupiter because of the outward-pointing co-rotating electric field (e.g. Horanyi et al. 1993). Within the first cycloid (within the first  $\sim 15$  minutes), when the grain is within  $\sim 10$  Io radii, both its direction and speed are comparable to the properties of the sodium jet. Grains of larger size (e.g. 100 nm), with a much smaller charge-to-mass ratio, are less accelerated by Lorentz forces compared to 10-nm-radius dust grains. Therefore, their velocity relative to Io is much smaller than the observed one. Similarly, much smaller particles (size  $< 10$  nm) have a much smaller gyroradius and tend to stay much closer to Io (a couple of Io radii at most) than our sodium feature. We shall return to this point in the next Section.

## 5. DISCUSSION

Nanodust particles get charged at high altitude at Io by capture of ionospheric electrons or photoelectron production (Krüger et al. 2003a). Only the most energetic plumes are expected to bring grains to high altitudes so that they collect sufficient charge from ambient plasma to overcome Io's gravity (Johnson et al. 1980). Flandes (2004) showed that particles need to reach at least  $\sim 400 \text{ km}$  altitude to be able to escape, and the flight time from vent to this height is 15-20 minutes.

Once they get charged, these nanodust particles follow trajectories that are determined by the corotational electric field of Jupiter's magnetosphere, in the radial direction. The dependence of dust trajectories on the highly variable magnetosphere in turn implies a certain variability in the expected dust flux with Jovian local time even if the dust ejection rate is constant. This variability, combined with the narrow field of view of our slit, might explain the variability seen in our dataset within a couple of hours (Figure 4). Most previous Io nanodust detection were carried out at distances further away from Io's orbit. In this respect, our observations probe a much closer region to Io than all previous dust measurements.

The spatial information of the observed Na jets also provides constraints on the dynamics of its possible dusty source. The observed Na speeds correspond roughly to  $\sim 50 \text{ km s}^{-1}$ , but grains in the dust model (10 nm in radius with  $20 e^-$  initial charge) need to be accelerated for some distance before reaching those speeds, at least  $7 R_{Io}$  as seen from Earth.

A dust grain with lower initial charge gets charged later, and thus farther away, and therefore its distance from Io would not match our observations. Only grains with proper charge-to-mass ratio can be sufficiently accelerated by the Lorentz forces and maintain a direction comparable to the observed sodium jet. To first order, regardless of the grain size, grains in the same plasma environment will be charged to roughly the same elec-

458 trostatic potential determined by the ambient plasma  
 459 conditions. For a given electrostatic potential, the grain  
 460 charge-to-mass ratio is inversely proportional to the  
 461 square of the grain size. Negatively charged grains much  
 462 larger than 10 nm have lower charge-to-mass ratio and  
 463 would not be accelerated to the observed speed in the  
 464 vicinity of Io. Negatively charged grains much smaller  
 465 than 10 nm, on the other hand, have much smaller gy-  
 466 roradius and will produce both red- and blue- shifted  
 467 components in the vicinity of Io, which is also not con-  
 468 sistent with the observation. The grain dynamics thus  
 469 suggests that the sodium jet can only be produced by  
 470 charged grains with radius  $\sim 10$  nm. This is in good  
 471 agreement with previous grain size estimate of the Jo-  
 472 vian stream particles based on space dust instruments  
 473 on board Galileo and Cassini spacecraft (Postberg et al.  
 474 2006; Hsu et al. 2012).

475 It is possible to perform a rough estimate of the source  
 476 rate from the spectra and compare it to the source rate  
 477 from the neutral model. The sodium source rate  $r$  is  
 478 the product of the peak column abundance, the vertical  
 479 extent  $d$  of the emission, and the velocity  $v_{\perp}$  perpen-  
 480 dicular to the observer’s line of sight (Schneider et al.  
 481 1991):

$$r = d \cdot v_{\perp} \cdot \int_{v_1}^{v_2} n(v) dv \quad (3)$$

482 In the above formula, we used Io’s diameter as verti-  
 483 cal extent  $d$  of our feature;  $n$  is the column density per  
 484 unit velocity averaged between 3.0 and 7.0  $R_{Io}$  and the  
 485 integral is performed between  $v_1 = 7$  and  $v_2 = 22$  km  
 486  $s^{-1}$  relative to Io, where the blueshifted feature is more  
 487 prominent. Finally, the velocity perpendicular to the  
 488 observer’s line of sight is defined as  $v_{\perp} = v_{los} \cdot \tan(\theta)$ ,  
 489 where  $v_{los}$  is the line-of-sight velocity (the one our spec-  
 490 troscopic observations are sensitive to) and  $\theta$  is the angle  
 491 between our line of sight and the jet (we assume our di-  
 492 rectional feature, or “jet”, to be the axis of the cone of  
 493 sodium atoms – see Figure 7). This angle is necessarily  
 494 taken out of our modeling, since with spectroscopic ob-  
 495 servations we can only measure the radial (line of sight)  
 496 velocity and have no information on the true orientation  
 497 of the sodium feature. For each spectrum, we average  
 498 the D2 and the D1 source rates and report these num-  
 499 bers in Table 2. The median of the resulting sodium  
 500 source rates is  $7.0 \times 10^{25}$  Na  $s^{-1}$  from the data, corre-  
 501 sponding to  $2.7$  kg  $s^{-1}$ . The source rate from the neutral  
 502 model is somehow greater ( $2.6 \times 10^{26}$  Na  $s^{-1}$ , correspond-  
 503 ing to  $10.0$  kg  $s^{-1}$ ), but this was derived assuming a wide  
 504 “jet” ( $30^{\circ}$  in the vertical direction). A narrower feature  
 505 would require proportionally less sodium.

### 5.1. Sputtering of Na from nanodust grains

**Table 2.** Sodium source rate for the emission feature dis-  
 cussed in this paper. The data source rate is the average of  
 the source rates from the D2 and D1 emission lines). Model  
 source rates for some of the April 2007 observations are not  
 available because the emission feature was not well defined.

filename	data source rate ( $s^{-1}$ )	model source rate ( $s^{-1}$ )
JDEI0119	$7.0 \times 10^{25}$	$1.6 \times 10^{26}$
JDEI0120	$1.1 \times 10^{26}$	$2.6 \times 10^{26}$
JDWF0002	$1.4 \times 10^{25}$	$5.8 \times 10^{25}$
JDWF0004	$2.8 \times 10^{25}$	$9.2 \times 10^{25}$
JDWF0008	$4.6 \times 10^{25}$	$1.4 \times 10^{26}$
JDWF0010	$7.0 \times 10^{25}$	$2.1 \times 10^{26}$
JDWF0015	$2.3 \times 10^{26}$	$2.9 \times 10^{26}$
JDWF0017	$1.7 \times 10^{26}$	$2.7 \times 10^{26}$
JDWF0022	$9.8 \times 10^{25}$	$2.8 \times 10^{26}$
JDWF0024	$7.7 \times 10^{25}$	$3.0 \times 10^{26}$
JDWF0025	$6.9 \times 10^{25}$	$2.2 \times 10^{26}$

507 For the dust hypothesis to work, we need a mechanism  
 508 that releases sodium atoms from these nanodust grains.  
 509 Possible processes include photon-stimulated desorption  
 510 (PSD), electron-stimulated desorption (ESD), or ion  
 511 sputtering. The first two have too low a source rate.  
 512 From experiments of PSD of Na from surfaces that sim-  
 513 ulate the lunar silicates (Yakshinskiy & Madey 1999),  
 514 scaling the solar flux to Jupiter’s distance, and taking  
 515 into account our derived distribution of dust grains, the  
 516 source rate from PSD is  $10^9$   $s^{-1}$ . The same authors also  
 517 showed that electron-stimulated desorption has an only  
 518 slightly higher cross section compared to PSD. The other  
 519 mechanism, ion sputtering, gives higher source rates, al-  
 520 though there are several uncertainties that affect the  
 521 calculation of the rate. First, an absolute value for  
 522 sputtering yield of sodium atoms has only been mea-  
 523 sured on  $Na_2S$ : Chrisney et al. (1988) report a sputtering  
 524 yield of 0.1 and 0.2  $Na_2S$  ion $^{-1}$  from  $O^+$  and  $S^+$  ions,  
 525 respectively. The molecules of interest in our case are  
 526 sodium chloride (NaCl) and sodium sulfate ( $Na_2SO_4$ ),  
 527 given that these were the compositions of the Na-bearing  
 528 dust grains detected by Cassini CDA (Postberg et al.  
 529 2006). Sodium sputtering yield for NaCl has been esti-  
 530 mated by Johnson (2000) to be  $\sim 1.0$  Na ion $^{-1}$ , assum-  
 531 ing that NaCl has the same atomic ejection efficiency  
 532 as  $Na_2S$ . Sodium sputtering yield for  $Na_2SO_4$  has only  
 533 been reported as a relative value: it is 100-1000 times  
 534 greater than the sputtering yield for NaS (Wiens et al.  
 535 1997). Assuming the absolute sputtering yield of NaS  
 536 to be the same as that of  $Na_2S$ , we can estimate the  
 537 Na sputtering yield from  $Na_2SO_4$  to be 100-1000 times  
 538 greater than that of NaCl, or 100-1000 Na ion $^{-1}$ . The

flux  $\Phi$  of precipitating ions responsible for the sputtering (mostly  $S^+$  and  $O^+$ ) can be calculated by multiplying the velocity of the ions (co-rotation, or  $57 \text{ km s}^{-1}$ ) by the density of these heavy ions close to Io, or about  $1500 \text{ cm}^{-3}$  (Dougherty et al. 2017). We obtain  $\Phi = 8.6 \times 10^9 \text{ cm}^{-2} \text{ s}^{-1}$ .

The second uncertainty is the dust available for sputtering. Over the course of the 7-year mission and from a distance between 13 and  $400 R_J$  from Io, the Galileo Dust Detector System (DDS) measured dust production rates at Io between  $10^{-3}$  and  $10^2 \text{ kg s}^{-1}$  (with an average value between  $0.1$  and  $1.0 \text{ kg s}^{-1}$ ), possibly correlated to volcanic eruptions at Io (Figure 2 of Krüger et al. 2003b).

With these numbers, we can estimate the number of Na atoms sputtered by nanodust grains and compare it to our observed sodium production rate. We start by assuming a dust production rate of  $1 \text{ kg s}^{-1}$ , the upper value of the average range reported by Krüger et al. (2003b). Assuming a spherical shape and a density of  $1.5 \text{ g cm}^{-3}$  (Krüger et al. 2003b), this corresponds to  $1.6 \times 10^{20}$  grains  $\text{s}^{-1}$  of radius  $10 \text{ nm}$ . We now multiply this number by the time it takes for the dust grains to reach the point where we do see sodium emission, or  $0.05$  hours (from Figure 9), to get  $N_{grains} = 2.9 \times 10^{22}$ . The total area available for sputtering will be  $N_{grains} \cdot A \cdot c$ , where  $A$  is the area of a  $10\text{-nm}$ -radius spherical nanodust grain, and  $c$  the concentration of either NaCl (90%) or  $\text{Na}_2\text{SO}_4$  (10%), from Cassini CDA measurements (Postberg et al. 2006). These areas are  $3.2 \times 10^{11} \text{ cm}^{-2}$  and  $3.6 \times 10^{10} \text{ cm}^{-2}$  for NaCl and  $\text{Na}_2\text{SO}_4$ , respectively. Multiplying them by the corresponding sputtering yields  $Y$  and the heavy ion flux, we get the sodium production rate for sputtering  $s$ :

$$s = N_{grains} \cdot A \cdot c \cdot \Phi \cdot Y \quad (4)$$

We obtain  $2.8 \times 10^{21} \text{ Na s}^{-1}$  from NaCl, and  $3.1 \times 10^{22} \text{ Na s}^{-1}$  from  $\text{Na}_2\text{SO}_4$  from  $1 \text{ kg s}^{-1}$  of dust material.

These numbers are between 3 and 4 orders of magnitude lower than our inferred rate of  $7.0 \times 10^{25} \text{ s}^{-1}$  (from the observations). They can be reconciled with our values if we assume some combination of the highest estimate for dust production rate from Galileo ( $100 \text{ kg s}^{-1}$ ), the highest estimate for the sputtering yield of Na from  $\text{Na}_2\text{SO}_4$  ( $1000 \text{ Na ion}^{-1}$ ), and a surface area for porous particles which is  $\sim 10$  times higher than the spherical area (this is the case for micron-sized lunar regolith particles; Taylor & Meek 2004). Additionally, the dust production rates from Galileo should be considered a lower limit, as dust is likely to undergo other destruction processes (not included in the calculations of Krüger et al. 2003b) between Io and the distance at

which grains were detected by Galileo (between 13 and  $400 R_J$  from Io). This is particularly true if some ejected dust has a more volatile composition than NaCl. Finally, it is not clear how the ion sputtering experiments, performed on flat surfaces, would change if the target is composed of nm-sized porous surfaces. To further investigate the discrepancy, a detailed calculation of the release of Na from dust particles and full treatment of dust destruction in Jupiter's highly complicated plasma environment would be required, and these are outside the scope of this paper.

We note that the new sodium feature was most prominent when Io was within  $5^\circ$  of the magnetic equator (Table 1). The bulk of the Io plasma torus is confined in the centrifugal equator, which is very close to the magnetic one. The plasma environment of that region (high plasma electron density and low electron temperature; Meyer-Vernet et al. 1995) is consistent with the negative grain charge polarity inferred from the trajectory simulation. In addition, the sputtering erosion responsible to release sodium atoms from dust surfaces is also higher at low magnetic latitudes because of the higher ion density. Our results thus indicate an indirect pathway to deliver sodium atoms, and likely other species, from Io to the Neutral Clouds (and ultimately to the magnetosphere) by sputtering from dust surfaces.

We conclude this section by evaluating and discarding another possible candidate, mentioned in Section 4.2, that is a population of negative ions formed inside Io's plumes. In this case, the most likely process to create these ions is three-body electron attachment. The most likely species to undergo this process is  $\text{NaSO}_4$ , a radical species with a substantial electron affinity and the highest rate coefficient among several Na-bearing species. The negative ions would then release the neutral sodium atoms we observe following electron detachment. The concentration of  $\text{NaSO}_4$  inside Io's plumes is unknown, but to match our observed source rate per unit volume, a density similar to that of potassium would be required, or 9 orders of magnitude greater than the expected concentration of  $\text{Na}_2\text{SO}_4$  inside Io's plumes (Moses et al. 2002). For this reason, we favor the hypothesis of ion sputtering from negatively charged dust nanograins as the most plausible source of our new sodium emission feature.

## 6. CONCLUSIONS

We have performed Monte Carlo simulation of sodium atoms under the influence of Io's gravity and solar radiation pressure to explain an unusual Jupiter-oriented feature (Schneider et al. 2008) we detected in our high-resolution spectra of Io's sodium Neutral Clouds from

640 the TNG telescope. This feature is directed towards  
 641 Jupiter and is rapidly variable in time. The best model  
 642 is the one that has the sodium atoms ejected in the  
 643 leading-sub/Jovian hemisphere of Io (45–68° West lon-  
 644 gitude) with a broad velocity distribution (50–90 km  
 645 s<sup>-1</sup>). We propose that the mechanism most likely re-  
 646 sponsible for creating sodium atoms with that orienta-  
 647 tion and that speed is sputtering of Na from Na-bearing  
 648 molecules (NaCl or Na<sub>2</sub>SO<sub>4</sub>, both detected near Jupiter  
 649 by Cassini CDA) attached to negatively charged dust  
 650 grains (10 nm in radius) that move under the influence  
 651 of the co-rotational electric field of Jupiter’s magne-  
 652 tosphere. This is consistent with modeling of trajectories  
 653 of negatively charged nanodust grains, which present the  
 654 right velocity and orientation consistent with our ob-  
 655 servations and our sodium model. The median sodium  
 656 source rate inferred from our observations is  $7.0 \times 10^{25}$   
 657 Na s<sup>-1</sup>, to be compared with the theoretical estimate  
 658 from ion sputtering of Na from NaCl or Na<sub>2</sub>SO<sub>4</sub> be-  
 659 tween  $5.5 \times 10^{21}$  Na s<sup>-1</sup> and  $6.2 \times 10^{26}$  Na s<sup>-1</sup>, depend-  
 660 ing on the choice of several uncertain parameters, such as  
 661 the sputtering yield, the dust production rate at Io, and  
 662 surface area available to sputtering. We point out the  
 663 need for detailed calculations of the release of Na from  
 664 dust particles and full treatment of dust destruction in  
 665 Jupiter’s highly complicated plasma environment.

666 Our results uncover a new mechanism by which Io’s  
 667 sodium Neutral Clouds are replenished, and highlight  
 668 the need for future observing campaigns to better con-  
 669 strain the escape rate of sodium atoms produced at Io  
 670 by this mechanism, before the arrival of Europa Clip-  
 671 per spacecraft, whose dust counter will be able to study  
 672 the dust population in the Jupiter environment at much  
 673 closer range than any other spacecraft so far.

#### 674 ACKNOWLEDGEMENTS

675 This work has been supported by NASA Solar Sys-  
 676 tem Workings grant 80NSSC18K0008, NSF’s Planetary  
 677 Astronomy Program, and the Astronomy Department  
 678 and CISAS of University of Padua, through a contract  
 679 by the Italian Space Agency (ASI). Cesare Grava wishes  
 680 to thank Rosemary M. Killen for providing the g-values  
 681 used in this work, and Jane L. Fox and John M. C.  
 682 Plane for insightful discussions on negative ions chem-  
 683 istry. Based on observations made with the Italian *Tele-*  
 684 *scopio Nazionale Galileo* (TNG) operated by the *Fun-*  
 685 *dación Galileo Galilei* of the *Istituto Nazionale di As-*  
 686 *trofisica* at the *Observatorio del Roque de los Mucha-*  
 687 *chos* (La Palma, Canary Islands, Spain). Files for ob-  
 688 servations in 2009 are available on the archive of the  
 689 TNG telescope, at <http://archives.ia2.inaf.it/tng>. Files  
 690 for observations in 2007 can be requested to the corre-  
 691 sponding author.

#### REFERENCES

- 692 Acton, C. H. 1996, *Planet. Space Sci.*, 44, 65,  
 693 doi: [10.1016/0032-0633\(95\)00107-7](https://doi.org/10.1016/0032-0633(95)00107-7)
- 694 Bagenal, F., & Dols, V. 2020, *Journal of Geophysical*  
 695 *Research (Space Physics)*, 125, e27485,  
 696 doi: [10.1029/2019JA027485](https://doi.org/10.1029/2019JA027485)
- 697 Brown, R. A. 1974, in *IAU Symposium*, Vol. 65,  
 698 *Exploration of the Planetary System*, ed. A. Woszczyk &  
 699 C. Iwaniszewska, 527–531
- 700 Brown, R. A., Goody, R. M., Murcray, F. J., & Chaffee,  
 701 F. H., J. 1975, *ApJL*, 200, L49, doi: [10.1086/181894](https://doi.org/10.1086/181894)
- 702 Brown, R. A., & Schneider, N. M. 1981, *Icarus*, 48, 519,  
 703 doi: [10.1016/0019-1035\(81\)90061-0](https://doi.org/10.1016/0019-1035(81)90061-0)
- 704 Brown, R. A., & Yung, Y. L. 1976, in *Jupiter*, 1102–1145
- 705 Burger, M. H., Killen, R. M., McClintock, W. E., et al.  
 706 2014, *Icarus*, 238, 51, doi: [10.1016/j.icarus.2014.04.049](https://doi.org/10.1016/j.icarus.2014.04.049)
- 707 Chrisey, D. B., Johnson, R. E., Boring, J. W., & Phipps,  
 708 J. A. 1988, *Icarus*, 75, 233,  
 709 doi: [10.1016/0019-1035\(88\)90003-6](https://doi.org/10.1016/0019-1035(88)90003-6)
- 710 Cremonese, G., Thomas, N., Barbieri, C., & Pernechele, C.  
 711 1992, *A&A*, 256, 286
- 712 Dougherty, L. P., Bodisch, K. M., & Bagenal, F. 2017,  
 713 *Journal of Geophysical Research (Space Physics)*, 122,  
 714 8257, doi: [10.1002/2017JA024053](https://doi.org/10.1002/2017JA024053)
- 715 Flandes, A. 2004, *Geophys. Res. Lett.*, 31, L16802,  
 716 doi: [10.1029/2004GL020046](https://doi.org/10.1029/2004GL020046)
- 717 Flynn, B., Mendillo, M., & Baumgardner, J. 1992, *Icarus*,  
 718 99, 115, doi: [10.1016/0019-1035\(92\)90176-8](https://doi.org/10.1016/0019-1035(92)90176-8)
- 719 Goldberg, B. A., Garneau, G. W., & Lavoie, S. K. 1984,  
 720 *Science*, 226, 512, doi: [10.1126/science.226.4674.512](https://doi.org/10.1126/science.226.4674.512)
- 721 Graps, A. L., Grün, E., Svedhem, H., et al. 2000, *Nature*,  
 722 405, 48, doi: [10.1038/35011008](https://doi.org/10.1038/35011008)
- 723 Grava, C., Schneider, N. M., Leblanc, F., et al. 2014,  
 724 *Journal of Geophysical Research (Planets)*, 119, 404,  
 725 doi: [10.1002/2013JE004504](https://doi.org/10.1002/2013JE004504)
- 726 Grün, E., Zook, H. A., Baguhl, M., et al. 1993, *Nature*, 362,  
 727 428, doi: [10.1038/362428a0](https://doi.org/10.1038/362428a0)
- 728 Grün, E., Baguhl, M., Hamilton, D. P., et al. 1996, *Nature*,  
 729 381, 395, doi: [10.1038/381395a0](https://doi.org/10.1038/381395a0)
- 730 Horányi, M., Grün, E., & Heck, A. 1997,  
 731 *Geophys. Res. Lett.*, 24, 2175, doi: [10.1029/97GL01539](https://doi.org/10.1029/97GL01539)

- 732 Horanyi, M., Morfill, G., & Grun, E. 1993, *Nature*, 363,  
733 144, doi: [10.1038/363144a0](https://doi.org/10.1038/363144a0)
- 734 Hsu, H.-W., Krüger, H., & Postberg, F. 2012, in *Nanodust*  
735 *in the Solar System: Discoveries and Interpretations*  
736 (Springer), 77–117
- 737 Hunten, D. M., Morgan, T. H., & Shemansky, D. E. 1988,  
738 *The Mercury atmosphere.*, ed. F. Vilas, C. R. Chapman,  
739 & M. S. Matthews, 562–612
- 740 Hunten, D. M., Roach, F. E., & Chamberlain, J. W. 1956,  
741 *Journal of Atmospheric and Terrestrial Physics*, 8, 345,  
742 doi: [10.1016/0021-9169\(56\)90111-8](https://doi.org/10.1016/0021-9169(56)90111-8)
- 743 Johnson, R. E. 2000, *Icarus*, 143, 429,  
744 doi: [10.1006/icar.1999.6327](https://doi.org/10.1006/icar.1999.6327)
- 745 Johnson, T. V., Morfill, G., & Grun, E. 1980,  
746 *Geophys. Res. Lett.*, 7, 305,  
747 doi: [10.1029/GL007i005p00305](https://doi.org/10.1029/GL007i005p00305)
- 748 Killen, R., Shemansky, D., & Mouawad, N. 2009, *ApJS*,  
749 181, 351, doi: [10.1088/0067-0049/181/2/351](https://doi.org/10.1088/0067-0049/181/2/351)
- 750 Krüger, H., Horányi, M., & Grün, E. 2003a,  
751 *Geophys. Res. Lett.*, 30, 1058,  
752 doi: [10.1029/2002GL015920](https://doi.org/10.1029/2002GL015920)
- 753 Krüger, H., Geissler, P., Horányi, M., et al. 2003b,  
754 *Geophys. Res. Lett.*, 30, 2101,  
755 doi: [10.1029/2003GL017827](https://doi.org/10.1029/2003GL017827)
- 756 Küppers, M., & Schneider, N. M. 2000,  
757 *Geophys. Res. Lett.*, 27, 513, doi: [10.1029/1999GL010718](https://doi.org/10.1029/1999GL010718)
- 758 Lellouch, E., Paubert, G., Moses, J. I., Schneider, N. M., &  
759 Strobel, D. F. 2003, *Nature*, 421, 45,  
760 doi: [10.1038/nature01292](https://doi.org/10.1038/nature01292)
- 761 Mendillo, M., Baumgardner, J., Flynn, B., & Hughes, W. J.  
762 1990, *Nature*, 348, 312, doi: [10.1038/348312a0](https://doi.org/10.1038/348312a0)
- 763 Meyer-Vernet, N., Moncuquet, M., & Hoang, S. 1995,  
764 *Icarus*, 116, 202, doi: [10.1006/icar.1995.1121](https://doi.org/10.1006/icar.1995.1121)
- 765 Moses, J. I., Zolotov, M. Y., & Fegley, B. 2002, *Icarus*, 156,  
766 107, doi: [10.1006/icar.2001.6759](https://doi.org/10.1006/icar.2001.6759)
- 767 Nash, D. B., Yoder, C. F., Carr, M. H., Gradie, J., &  
768 Hunten, D. M. 1986, *Io*, ed. J. A. Burns & M. S.  
769 Matthews, 629–688
- 770 Postberg, F., Kempf, S., Srama, R., et al. 2006, *Icarus*, 183,  
771 122, doi: [10.1016/j.icarus.2006.02.001](https://doi.org/10.1016/j.icarus.2006.02.001)
- 772 Schneider, N. M., & Bagenal, F. 2007, *Io's neutral clouds,*  
773 *plasma torus, and magnetospheric interaction*, ed.  
774 R. M. C. Lopes & J. R. Spencer, 265,  
775 doi: [10.1007/978-3-540-48841-5\\_11](https://doi.org/10.1007/978-3-540-48841-5_11)
- 776 Schneider, N. M., Grava, C., & Barbieri, C. 2008, in  
777 *AAS/Division for Planetary Sciences Meeting Abstracts*  
778 *#40, AAS/Division for Planetary Sciences Meeting*  
779 *Abstracts*, 59.09
- 780 Schneider, N. M., Trauger, J. T., Wilson, J. K., et al. 1991,  
781 *Science*, 253, 1394, doi: [10.1126/science.253.5026.1394](https://doi.org/10.1126/science.253.5026.1394)
- 782 Taylor, L. A., & Meek, T. T. 2004, in *International Lunar*  
783 *Conference 2003*, ed. S. M. Durst, C. T. Bohannon, C. G.  
784 Thomason, M. R. Cerney, & L. Yuen, Vol. 108, 109
- 785 Trafton, L. 1975, *ApJL*, 202, L107, doi: [10.1086/181991](https://doi.org/10.1086/181991)
- 786 Trafton, L., & Macy, W., J. 1977, *ApJ*, 215, 971,  
787 doi: [10.1086/155433](https://doi.org/10.1086/155433)
- 788 Trafton, L., & Macy, W. 1978, *Icarus*, 33, 322,  
789 doi: [10.1016/0019-1035\(78\)90152-5](https://doi.org/10.1016/0019-1035(78)90152-5)
- 790 Trafton, L., Parkinson, T., & Macy, W., J. 1974, *ApJL*,  
791 190, L85, doi: [10.1086/181512](https://doi.org/10.1086/181512)
- 792 Wiens, R. C., Burnett, D. S., Calaway, W. F., et al. 1997,  
793 *Icarus*, 128, 386, doi: [10.1006/icar.1997.5758](https://doi.org/10.1006/icar.1997.5758)
- 794 Wilson, J. K., & Schneider, N. M. 1994, *Icarus*, 111, 31,  
795 doi: [10.1006/icar.1994.1131](https://doi.org/10.1006/icar.1994.1131)
- 796 —. 1999, *J. Geophys. Res.*, 104, 16567,  
797 doi: [10.1029/1999JE900017](https://doi.org/10.1029/1999JE900017)
- 798 Yakshinskiy, B. V., & Madey, T. E. 1999, *Nature*, 400, 642,  
799 doi: [10.1038/23204](https://doi.org/10.1038/23204)
- 800 Zhang, J., Goldstein, D. B., Varghese, P. L., et al. 2004,  
801 *Icarus*, 172, 479, doi: [10.1016/j.icarus.2004.06.016](https://doi.org/10.1016/j.icarus.2004.06.016)
- 802 Zook, H. A., Grun, E., Baguhl, M., et al. 1996, *Science*,  
803 274, 1501, doi: [10.1126/science.274.5292.1501](https://doi.org/10.1126/science.274.5292.1501)